Gradient nano microstructure and its formation mechanism in pure titanium produced by surface rolling treatment

Qi Wang, Yanfei Yin, Qiaoyan Sun, Lin Xiao,[a] and Jun Sun
State Key Laboratory for Mechanical Behavior of Materials, Xi'an Jiaotong University, Xi'an, Shaanxi 710049, People's Republic of China

(Received 1 September 2013; accepted 13 January 2014)

A large depth of 800 μm gradient microstructure was produced in pure titanium (Ti) by means of surface rolling treatment (SRT). The microstructural characteristics with different depths from the top surface were analyzed by optical microscopy, transmission electron microscopy, and electron backscattered diffraction. The results showed that, on the outmost surface, nanograins with an average grain size of ~100 nm were achieved. In the subsurface, i.e., the deformation twinning region, a large volume fraction of $\{10\bar{1}2\}$ deformation twins together with a low fraction of $\{11\bar{2}2\}$ and $\{11\bar{2}4\}$ twins were identified. Based on the microstructural analysis, the grain refinement mechanisms with increasing strain are summarized as: (i) prior division by deformation twinning, (ii) refinement effect of subgrain boundaries resulting from the accumulation of high density of dislocation, and (iii) transformation effect from low angle grain boundaries to high angle grain boundaries. The results of tension tests also show that the titanium sample after SRT shows higher strength than the as-received titanium sample.

I. INTRODUCTION

Commercial-purity titanium (Ti) has been widely used in medical industry owing to its high ratio of strength and weight, high corrosion resistance, and excellent biocompatibility.[1] However, it has a low yield stress, ultimate strength, and fatigue limit due to its coarse grain (CG) size, which restricts its application. According to the Hall–Petch law,[2,3] grain refinement is an effective way to enhance both strength and ductility of metals and alloys. Severe plastic deformation (SPD), including equal channel angular pressing (ECAP), high press torsion, accumulative roll-bonding (ARB),[4] and surface nanocrystallization (SNC),[5] has proved to be one of the effective techniques to produce ultrafine grains (UFG, 100 nm $< d <$ 1000 nm) and nanograins (NG, $d <$ 100 nm).[6] The strength of UFG/NG materials produced by SPD can be significantly improved. Recent research[7,8] shows that a gradient UFG/NG microstructure produced on the surface of Ti by SNC can possess excellent strength and fatigue life. The results in literature[9] demonstrated that the gradient UFG/NG layer has a crack-stopping effect to prevent catastrophic failure. Wen et al.[10] found that the pure Ti after a two-step treatment including surface mechanical attrition treatment (SMAT) combined with thermal oxidation process showed excellent wear-resistance and biocompatibility.

The SNC technique includes shot peening, cryogenic burnishing, SMAT, surface mechanical grinding treatment (SMGT),[11] and low plasticity burnishing.[12,13] The SPD behavior of Ti has been extensively studied during ECAP[14] and ARB,[15] which are often carried out at 450–500 °C to avoid the billet to be broken. In fact, the dislocation slip and shear bands are activated, and the deformation twinning is suppressed at this range of temperature during plastic deformation.[16,17] Twinning is an important deformation mode in HCP Ti, specifically at high strain rate and low temperature. Numerous studies have proved that deformation twinning can accelerate the grain refinement process.[18,19] Recently, the UFG/NG Ti has been fabricated by ECAP at room temperature by increasing the channel angle of the die and using a relatively slow ram speed.[20] However, little attention is paid to the difference of refinement mechanism between room temperature and the elevated temperature. Although the effect of deformation twinning on grain refinement in pure Ti at room temperature has been investigated by Lu et al.[21] during SMAT, further quantitative information is needed. The objective of this paper is to supply more details for the refinement of grains in the surface and subsurface of titanium with a large depth of gradient structure in hcp Ti fabricated by the surface rolling treatment (SRT) by analysis of x-ray diffraction (XRD), optical microscopy (OM), transmission electron microscope (TEM), EBSD, and microhardness. The evolution of microstructure with different depths from the treated surface was characterized. Special attention is paid to the role of twinning and dislocations in refining grain size. Grain refinement mechanisms at different depths from the surface were summarized based on analysis of the substructure.

[a]Address all correspondence to this author.
e-mail: lxiao@mail.xjtu.edu.cn
DOI: 10.1557/jmr.2014.19

 © Materials Research Society 2014

https://doi.org/10.1557/jmr.2014.19 Published online by Cambridge University Press

II. EXPERIMENTAL PROCEDURE

The material used in this study is the annealed commercial-purity Ti bars of 16 mm in diameter, with an average grain size of ~30 μm. To obtain a nanostructure on the surface, a specific combination of ball and bearing was designed, as schematically illustrated in Fig. 1. This technique is similar to the SMGT technology, to some extent, which was invented by Lu et al.,[11,22] except replacing the turning tool with a moving ball. The Ti bars were processed by means of SRT at room temperature. The effect of different parameters on the microstructure and microhardness was first investigated by optical microscopy observation and microhardness test. For example, the results of pure Ti fabricated with different passes are shown in Fig. 2. It is observed that the sample obtained a deeper refined microstructural region after ten passes treated than five passes. Meanwhile, the surface microhardness increases from 354 to 432 Hv. Finally, the optimized parameters for pure Ti are determined: the rotation velocity of samples v_1 = 630 rpm, horizontal travel speed of the ball v_2 = 1 mm/s, and the rolling depth of the ball into the sample every time a_p = 50 μm. The SRT was continuously repeated ten times with the same process parameters so as to achieve a thick and uniform nanograined layer. We have just conducted tension tests on the SRTed titanium sample and untreated sample. The strength and elongation to the fracture are given in Table I together with hardness.

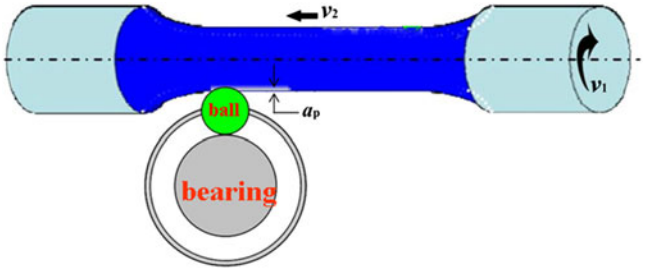


FIG. 1. Schematic illustration of SRT.

XRD analysis on the surface layer of SRT samples was carried out on a Rigaku D/max x-ray diffractometer (12 Kw; Japan) with a Cu K_α radiation. Small angular steps of 2θ = 0.02° and accounting time of 20 s were used to measure the width of a diffraction peak in a step-scanning mode.

The microstructural evolution of SRT samples was characterized using Olympus OLS4000 OM and JEM-200CX TEM (Japan). Metallographic samples were immersed in a solution of 2% (volume) HF, 8% HNO_3, and 90% H_2O for 10–15 s and immediately washed with water. Different subsurface layers were mechanically ground from the untreated side to ~50 μm in thickness and then electropolished using a twin-jet technique in a solution of 60% methanol (volume %), 35% butyl alcohol, and 5% perchloric acid at a voltage of 10–15 V and a temperature of about −30 °C. Electron backscatter diffraction (EBSD) was used to characterize the type of deformation twinning.

III. RESULTS

A. XRD analysis

XRD analysis results of the surface layer in CG and SRTed Ti are shown in Fig. 3(a). Bragg diffraction peaks were broadened in SRTed sample compared with the as-received Ti. The similar characteristic was observed in other SPD metals and alloys.[23] The Bragg diffraction peak broadening could be attributed to the effect of grain refinement and microstrain increase in lattice scale. The relationship between the grain refinement broadening and microstrain broadening can be approximately expressed by the Scherrer equation[24]:

$$\beta \cos\theta = (k\lambda/d) + \varepsilon \sin\theta \quad , \qquad (1)$$

where β is the measured integral breadth, θ is the peak maximum position, d is the grain size, ε is the microstrain, λ is the wave length, and k is a constant. Figure 3(b) showed a linear regression relationship between βcosθ/λ and sinθ/λ for all measured peaks of the SRTed samples. According to Eq. (1), grain size and microstrain are equal to the reciprocal

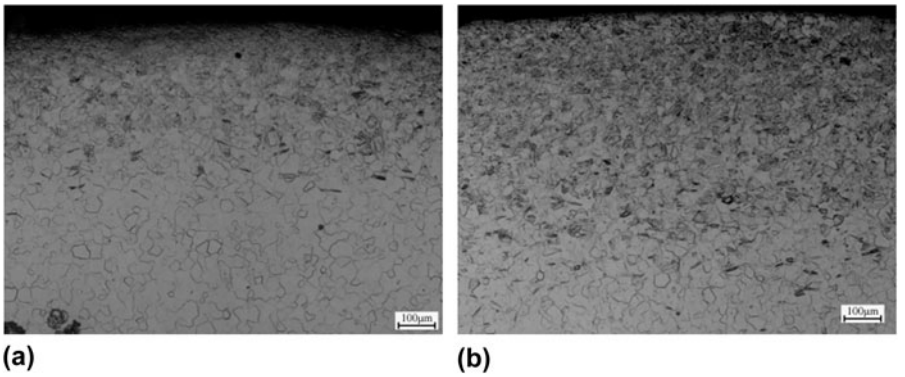


FIG. 2. The optical microstructure of Ti sample fabricated by SRT with five passes (a) and ten passes (b).

https://doi.org/10.1557/jmr.2014.19 Published online by Cambridge University Press

of intercept and the slope of regression line, respectively.[25] Figure 3(b) shows that the average grain size is about 72 nm when the microstrain is about 0.51%.

B. Optical and TEM microstructural observation

Optical microstructure in SRTed Ti is shown in Fig. 4. A gradient structure of 800 μm in depth was obtained as the depth increased from the treated surface. The gradient structure can be further divided into three regions. In the outmost of 100 μm (region I), the grain boundaries were obscure. It indicates that the CGs have been refined into ultrafine or nanoscale, which will be further confirmed by the following TEM images. To the authors' knowledge, such a depth of nanostructure in Ti has not been reported in other SNC treatments, such as SMAT, SMGT, and shot peening.[7,8] In a depth of 100–800 μm (region Π), the microstructure gradually transformed into the deformed CGs, which were characterized by plenty of deformation twinning. The density of deformation twinning decreased as the depth increased. When the depth is larger than 800 μm (region Ш), the microstructure remains CG matrix. Similar results were also observed in SMATed Ti.[21,26]

TABLE I. The mechanical properties of pure Ti before and after SRT.

	σ_y (MPa)	σ_{UTS} (MPa)	Elongation to fracture (%)	Microhardness (HV)
CG Ti	380	451	24	163
SRT Ti	437	495	21	434

The microstructure at different depths was further examined with TEM. Figures 5(a) and 5(b) show the bright and dark fields of TEM images and the corresponding selected-area electron diffraction pattern (SADP) in SRTed Ti at a depth of ~50 μm. The microstructure is mainly composed of ultrafine grains and nanograins [Fig. 5(a)]. Nanograins are almost characterized with curved grain boundaries with a high density of dislocations in most grains. The SADP exhibits well-defined rings, which suggest that nanograins are highly disoriented with respect to each other. Figure 5(c) shows the histogram map of grain size distribution obtained from a bright field image and at least four dark field images. It is demonstrated that the grain size at a depth of ~50 μm subsurface ranges from 50 to 300 nm with an average grain size of 95 nm.

Microstructural feature on the topmost layer is shown in Fig. 6(a). In comparison with the micrograph in Fig. 5(a), the nanograins are more defined and equiaxed. Dislocation density was significantly reduced. This indicates that continuous dynamic recrystallization (CDRX) took place. As a result, dislocations rearranged and internal stresses decreased; but extra grain growth did not occur, as shown in Fig. 6(b).

The bright field TEM images in SRTed Ti at the depth of ~400 μm are shown in Figs. 7(a) and 7(b). Deformation twin is the major microstructural features

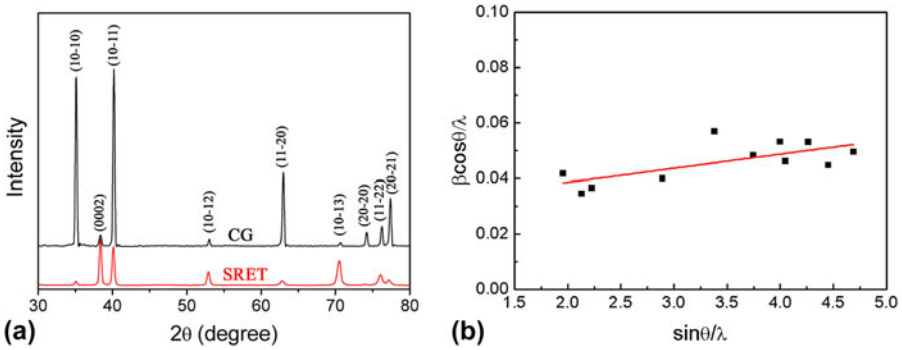


FIG. 3. XRD results of the surface layer in coarse-grained and SRTed Ti (a) XRD curves and (b) the relationship between βcosθ/λ and sinθ/λ.

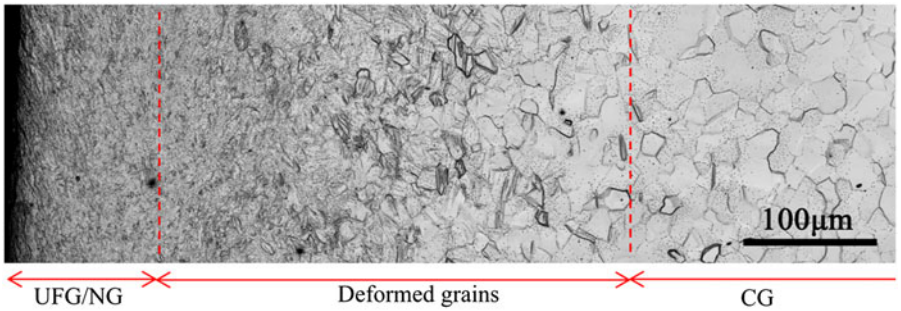


FIG. 4. Optical micrograph in the cross-section of the SRTed Ti.

https://doi.org/10.1557/jmr.2014.19 Published online by Cambridge University Press

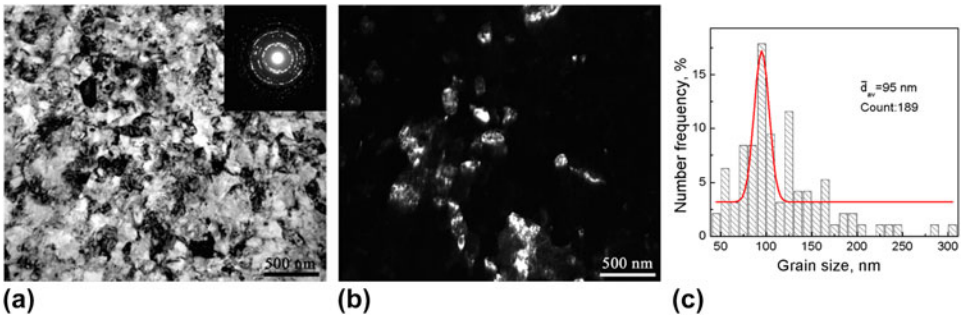


FIG. 5. TEM microstructure and the corresponding grain size distribution at the outmost depth of 50 nm in the SRTed Ti: (a) bright field (the inset is the SADP), (b) dark field, and (c) grain size distribution map.

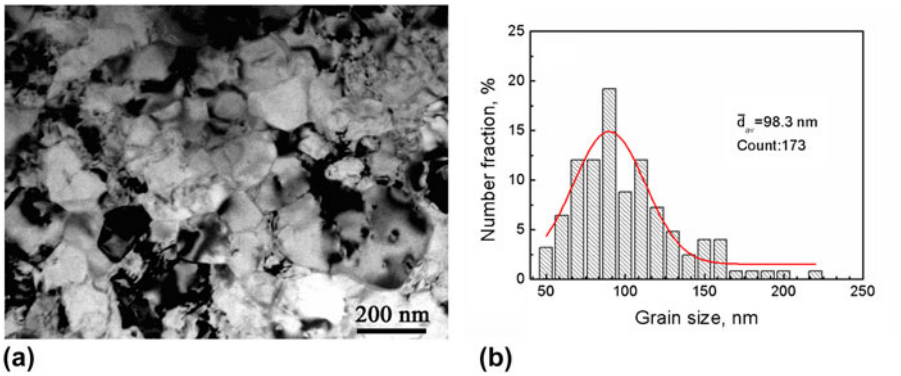


FIG. 6. TEM image (a) and the corresponding grain size distribution (b) in SRTed Ti at a depth of ~10 μm.

at this depth. Some twin–twin intersection and twin–dislocation interaction were observed. In Fig. 7(a), two sets of deformation twins intersect with each other and ultimately refine the microstructure into irregular shape of nanograins. In Fig. 7(b), several dislocation walls perpendicular to the twin boundary were formed within the deformation twins due to the accumulation of a plenty of dislocations, as indicated by arrows in Fig. 7(b). Meanwhile, these dislocation walls broke deformation twins into rhomboid blocks.

TABLE II. The misorientations angle along the axis and Schmid factors for different deformation twins in Ti.

Twin type	Twinning systems	Misorientation angle/axis	Schmid factors
Tensile twin	$\{11\bar{2}1\}<11\bar{2}6>$	34.96° $<1\bar{1}00>$	0.29
	$\{10\bar{1}2\}<10\bar{1}1>$	84.78° $<11\bar{2}0>$	0.50
	$\{11\bar{2}3\}<33\bar{6}2>$	86.98° $<1\bar{1}00>$	0.23
Compressive twin	$\{10\bar{1}1\}<10\bar{1}2>$	61.38° $<11\bar{2}0>$	0.42
	$\{11\bar{2}2\}<11\bar{2}3>$	64.43° $<1\bar{1}00>$	0.45
	$\{11\bar{2}4\}<22\bar{4}3>$	76.86° $<1\bar{1}00>$	0.49

C. EBSD analysis of microstructure

Six types of twins, including $\{11\bar{2}1\}$, $\{10\bar{1}2\}$, $\{11\bar{2}3\}$, $\{10\bar{1}1\}$, $\{11\bar{2}2\}$, and $\{11\bar{2}4\}$, have been observed in the deformed Ti, as listed in Table II.[22,26] To determine the evolution of deformation twinning and the boundary misorientations with the distance from the treated surface in the SRTed Ti, the EBSD was used to characterize the microstructure. Figure 8 demonstrates the EBSD results in the CG at the depth of ~600 μm. There are plenty of deformation twins in the selected grains. Grains were subdivided into several segments by twin boundaries, as shown in Fig. 8(a). All boundaries formed by twinning are large angle grain boundaries, as shown in Fig. 8(b). In comparison, some low angle grain boundaries (LAGBs) were formed due to dislocations accumulation. The volume fraction of the low angle boundaries is smaller than the large angle grain boundaries produced by twinning [Fig. 8(b)]. This indicates that twinning is the dominant deformation mode at this depth. In Fig. 8(c), different types of deformation twinning boundaries were marked by different colors. Black lines indicate high angle boundaries ($\theta > 15°$) and red line indicates low angle boundaries ($5°<\theta < 15°$). $\{10\bar{1}2\}<10\bar{1}1>$ twinning and a small amount of $\{11\bar{2}2\}<11\bar{2}3>$ and $\{11\bar{2}4\}<22\bar{4}3>$ were observed in the selected grain. On close examination, the $\{10\bar{1}2\}<10\bar{1}1>$ tensile twins were parallel to each other and encompassed inside the entire grain. In some case, the $\{10\bar{1}2\}<10\bar{1}1>$ tensile twins also intersected with each other, as indicated by a black square in Fig. 8(c).

https://doi.org/10.1557/jmr.2014.19 Published online by Cambridge University Press

The EBSD inverse pole map and the grain boundary map at the depth of ~300 μm are shown in Figs. 9(a) and 9(b), respectively. It contains a large number of ultrafine grains inside the twinned bands, which are formed by different types of twin intersections and secondary twins [Fig. 9(a)]. As deformation twinning became saturated with strain increasing, the pyramidal and prismatic slip played an important role in maintaining a homogeneous plastic deformation. The dislocation cells or subgrains were formed by the dislocation–dislocation interactions, dislocation–twins boundaries interactions. Dislocations were accumulated in the vicinity of twinning bands. This result can be proved by the corresponding grain boundary mapping, as shown in Fig. 9(b). There exist a large number of low angle boundaries colored in red inside twinning bands. This indicates that a great amount of dislocation slip took place.

The EBSD inverse pole map and the grain boundary map at the depth of ~100 μm are shown in Figs. 10(a) and 9(b), respectively. It was clearly seen that the initial grains

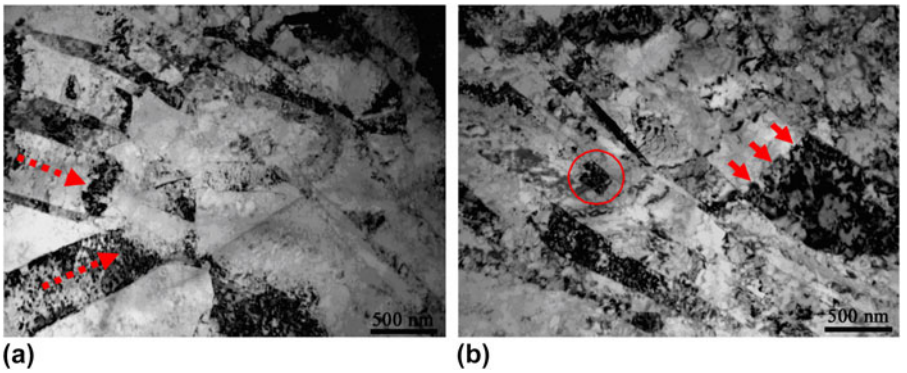


FIG. 7. TEM microstructure in the SRTed Ti at a depth of ~400 μm (a) twin–twin intersection and (b) twin–dislocation interaction.

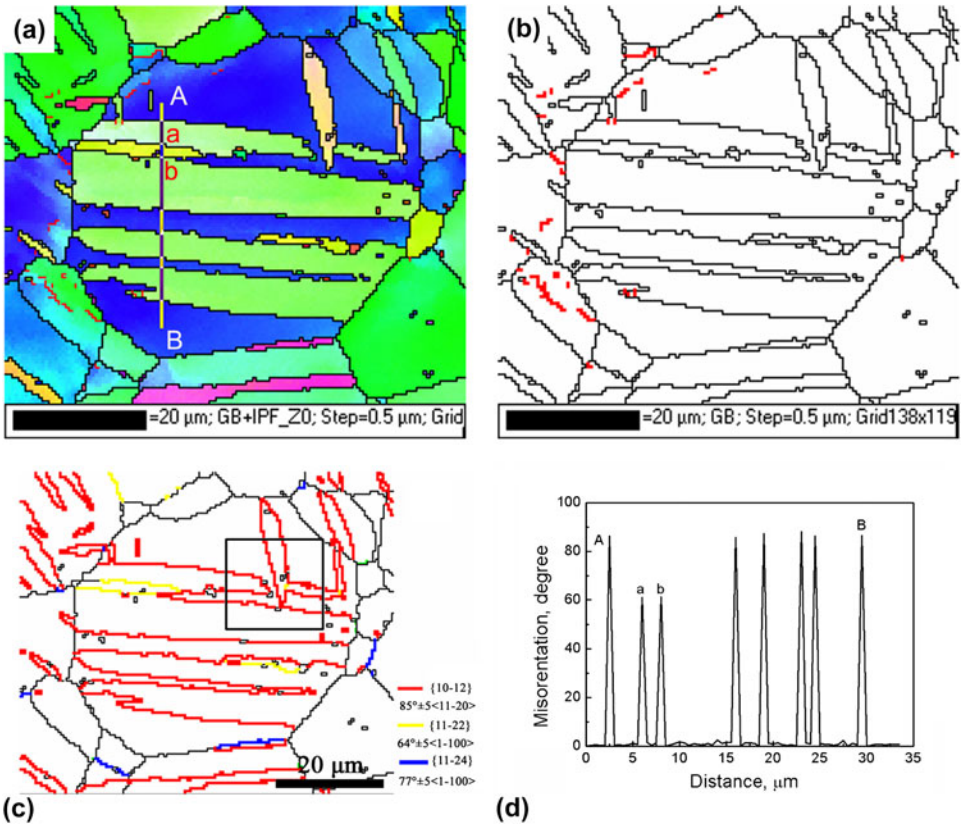


FIG. 8. EBSD results in the CG region at a depth of ~600 μm: (a) inverse pole figure map, (b) boundary map, and (c) different types of twin boundary map. Black lines indicate high angle boundaries ($\theta > 15°$) and red line indicates low angle boundaries ($5° < \theta < 15°$), and (d) Point-to-point misorientation line profile along the direction of line AB in (a).

https://doi.org/10.1557/jmr.2014.19 Published online by Cambridge University Press

have also been refined to submicrometer similar to the microstructure at a depth of ~300 μm. However, the fraction of low angle boundaries sharply decreases. In other words, with increasing strain, the misorientations of dislocation cells and subgrain boundaries increased, leading ultimately to the formation of high angle boundaries.

Figure 11 describes the corresponding misorientation angle distribution in the above EBSD maps. At the depth of ~600 μm, some peaks of grain boundary misorientations were observed at about 30, 64, 76, and 85°, respectively, as shown in Fig. 11(a). The peaks of 64, 76, and 85° were ascribed to the $\{10\bar{1}2\}$, $\{11\bar{2}4\}$, and $\{11\bar{2}2\}$ twinning systems. However, the formation mechanism of peak at about 30° is still unclear.[27] The volume fraction of $\{10\bar{1}2\}$ twin is larger than that of $\{11\bar{2}4\}$ and $\{11\bar{2}2\}$ twins. This suggested that the $\{10\bar{2}1\}$ twins were mainly activated at initial deformation due to their low critical resolved shear stress.[28,29] At the depth of ~300 μm [Fig. 11(b)], as the dislocations slip became the dominant deformation mode, the formation of dislocation walls and cells resulted in the increase of low angle boundaries. With strain increasing, the low angle boundaries transform into the high angle boundaries, as shown in Fig. 11(c). Meanwhile, the volume fraction of twin decreases as the twinning areas lost coherency with the matrix.

IV. DISCUSSION

Based on different microstructural characterization techniques, the grain or subgrain size as a function of the distance from the surface can be summarized in four regions, as shown in Fig. 12. Three different grain refinement mechanisms could be clarified.

A. Twinning division and subdivision refinement

According to the Zener–Hollomon criterion,[30,31] the deformation twinning takes place in the early stage of deformation in hcp Ti. Six different types of twinning have been observed in pure Ti (Table II).[22,27] The selective criterion of different twinning systems has been investigated by many researchers.[32,33] With the highest Schmid factor, $\{10\bar{1}2\}$ twin is easier to be activated than other types of twins at the same deformation condition. Meanwhile, its volume fraction is large. They nucleate and propagate quickly inside the entire grain. The initial grains are divided into several finer grains by twinning boundaries [Fig. 8(a)]. Here, the new twinning region and the remained matrix can be considered as different independent grains. The corresponding grain/subgrain size distribution at this stage is located in the region III of Fig. 12. The transverse size sharply decreases and directly depends on the thickness of deformation twinning, while the longitudinal size

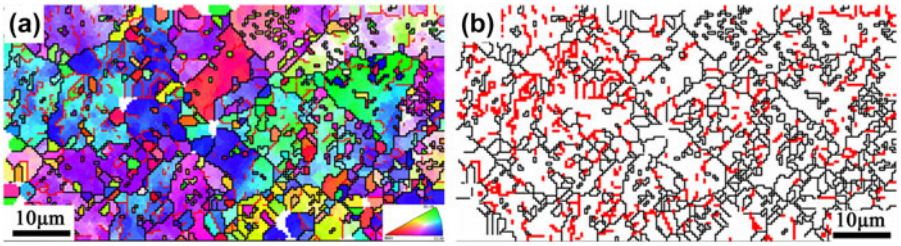


FIG. 9. EBSD inverse pole figure map at a depth of ~300 μm (a) and the corresponding boundary mapping (b). [High angle boundaries ($\theta > 15°$) are colored in black and low angle boundaries ($5° < \theta < 15°$) are colored in red.]

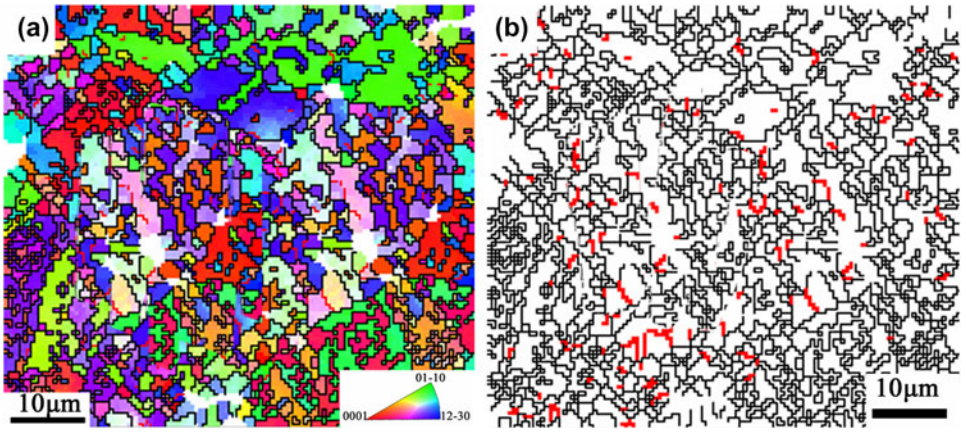


FIG. 10. EBSD inverse pole figure map at a depth of ~300 μm (a) and the corresponding boundary map (b). [High angle boundaries ($\theta > 15°$) are colored in black and low angle boundaries ($5° < \theta < 15°$) are colored in red.]

https://doi.org/10.1557/jmr.2014.19 Published online by Cambridge University Press

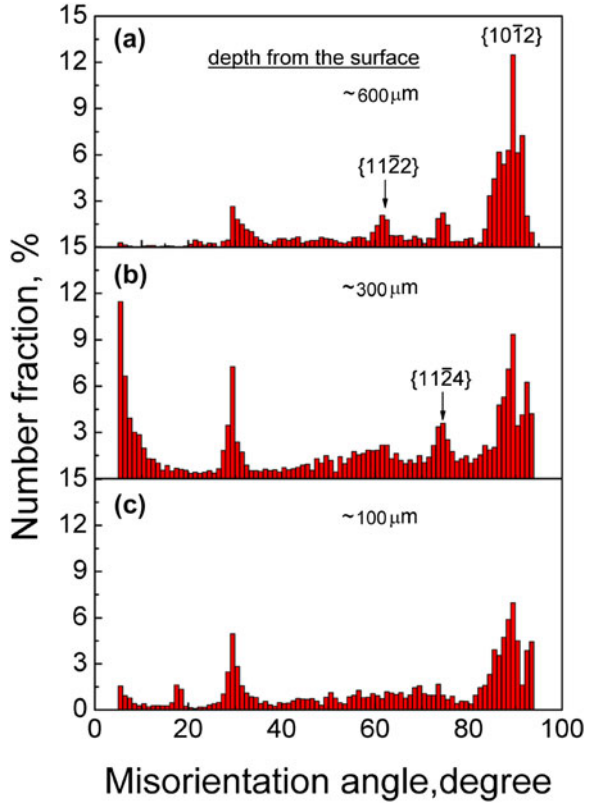


FIG. 11. Misorientations distribution at different depths from the surface: (a) ~600 μm, (b) ~300 μm, and (c) ~100 μm.

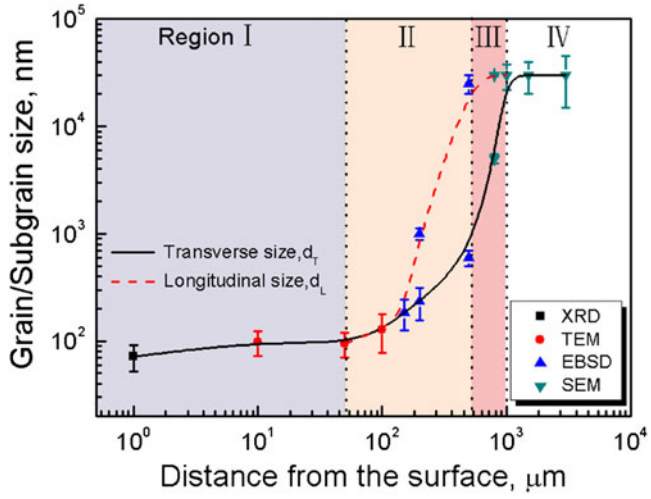


FIG. 12. The grain/subgrain size as a function of the distance from the surface.

decreased gently and the value is nearly equal to the initial grain size. With the strain increasing, the twins with the lower Schmid factors such as {11$\bar{2}$2} and {11$\bar{2}$4} gradually appear and the remained matrix is successively segmented. It is worth noting that the number of twinning with the lower Schmid factor is obviously fewer, and its thickness is narrower than that of {10$\bar{1}$2} twinning [Fig. 8(d)]. Occasionally, when the orientation of twinning areas is suitable for subsequent further twinning, the secondary twins or tertiary twins could be activated inside the primary twins.[34,35] This results in the fragmentation of the primary twins. Moreover, the various deformation twinning systems may intersect with each other [Fig. 7(a)].

B. Grain refinement due to dislocation accumulation

It has demonstrated that twinning deformation mechanism is sensitive to the grain size.[18] The formation of fresh twins becomes difficult as the grain size reduces to a critical value.[36,37] The volume fraction of deformation twinning reaches to a saturation value with the increase in strain. The twinning subdivision effectiveness is no longer active. Dislocation slip becomes a dominant plastic deformation mode.[21,38] Subgrains or dislocation cells will be formed inside the twinning area and the remained matrix via dislocation slip process [Fig. 7(b)]. In the area of twinning, dislocations walls were formed as the dislocations accumulated. They usually are perpendicular to the twinning boundaries. The twinning grains were broken into several segments due to the formation of the dislocations walls. Extensive investigations show that the mean diameter of subgrains formed by this process depends on the thickness of twins.[39] As a result, the size of a subgrain due to the fragmentation of twins with a high Schmid factor is larger than that with a low Schmid factor. In the remained matrix, various slip systems including pyramidal and prismatic slip will be activated to accommodate the further plastic deformation. A plenty of dislocations activities led to the formation of dislocation walls and tangles. These dislocation configurations will gradually subdivide the remained matrix by forming individual dislocation cells [Fig. 7(b)].

C. The evolution of LAGBs to HAGBs

Subgrain or dislocation cells are typical LAGBs. With the further increase of strain, the LAGBs can transform into high angle grain boundaries (HAGBs). The LAGBs movement is driven by stress, which has been systematically investigated from the perspective of experiments,[40] dislocation dynamics simulation,[41] and molecular dynamics simulation.[42,43] The stress-driving migration of LAGBs ultimately leads to the formation of HAGBs. Since the pure Ti has a high stacking-fault energy,[44] some amount of adiabatic heat may produce on the outmost treated surface during SPD. Therefore, CDRX could occur [Fig. 6(a)]. Consequently, LAGBs evolve into HAGBs with the progressive increasing of misorientation of LAGBs.[45,46] However, the subgrains or cells do not show an obvious growth with the increase of misorientation, as shown in the region I of Fig. 12.

https://doi.org/10.1557/jmr.2014.19 Published online by Cambridge University Press

V. CONCLUSIONS

(1) A depth of 800 μm of gradient nano structure was produced in pure Ti by means of SRT.

(2) The gradient structure can be divided into three regions. In the outmost depth of 100 μm, nanograins with an average grain size of ~100 nm were achieved. In a depth span of 100–800 μm, a large number of twins were observed. In the depth over 800 μm, the initial CGs were kept.

(3) Three different types of deformation twinning, including a large volume fraction of {10-12} <10-11> and a low fraction of {11-22} <11-23>, {11-24} <22-43>, were observed in the deformed grain regions.

(4) The grain refinement mechanism can be summarized as prior refinement by deformation twinning, grain refinement due to dislocation accumulation effect, and the evolution of LAGBs into HAGBs.

ACKNOWLEDGMENTS

This project was financially supported by the National Natural Science Foundation of China (Grant Nos. 51071118, 51271136, 50831004, and 51321003), the 973 Program of China (Grant Nos. 2010CB631003 and 2014CB644003), and the 111 Project of China (Grant No. B06025).

REFERENCES

1. I-S. Lee, D-H. Kim, H-E. Kim, Y-C. Jung, and C-H. Han: Biological performance of calcium phosphate films formed on commercially pure Ti by electron-beam evaporation. *Biomaterials* **23**, 609 (2002).
2. E.O. Hall: The deformation and ageing of mild steel: III discussion of results. *Phys. Soc. B* **64**, 747 (1951).
3. N.J. Petch and J. Lron: The cleavage strength of polycrystals. *Steel Inst.* **174**, 25 (1953).
4. R.Z. Valiev, R.K. Islamgaliev, and I.V. Alexandrov: Bulk nanostructured materials from severe plastic deformation. *Prog. Mater. Sci.* **45**, 103 (2000).
5. N.R. Tao, Z.B. Wang, W.P. Tong, M.L. Sui, J. Lu, and K. Lu: An investigation of surface nanocrystallization mechanism in Fe induced by surface mechanical attrition treatment. *Acta Mater.* **50**, 4603 (2002).
6. Y.M. Wang and E. Ma: High tensile ductility in a nanostructured metal. *Appl. Phys. Lett.* **80**, 2395 (2002).
7. T. Roland, D. Retraint, K. Lu, and J. Lu: Fatigue life improvement through surface nanostructuring of stainless steel by means of surface mechanical attrition treatment. *Scr. Mater.* **54**, 1949 (2006).
8. T.H. Fang, W.L. Li, N.R. Tao, and K. Lu: Revealing extraordinary intrinsic tensile plasticity in gradient nano-grained copper. *Science* **331**, 1587 (2011).
9. D.K. Yang and P.D. Hodgson: Tough ultrafine-grained Ti through multilayering and grading. *Scr. Mater.* **68**, 309 (2013).
10. M. Wen, C. Wen, P. Hodgson, and Y. Li: Improvement of the biomedical properties of titanium using SMAT and thermal oxidation. *Colloids Surf., B* (2013, in press).
11. J. Li and A.K. Soh: Modeling of the plastic deformation of nanostructured materials with grain size gradient. *Int. J. Plast.* **39**, 88 (2012).
12. R. Avilés, J. Albizuri, A. Rodríguez, and L.N. López de Lacalle: Influence of low-plasticity ball burnishing on the high-cycle-fatigue strength of medium carbon AISI 1045 steel. *Int. J. Fatigue* **55**, 230 (2013).
13. P.S. Prevéy and J.T. Cammett: The influence of surface enhancement by low plasticity burnishing on the corrosion fatigue performance of AA7075-T6. *Int. J. Fatigue* **26**, 975 (2004).
14. S.S. Dheda and F.A. Mohamed: Effect of initial microstructure on the processing of titanium using equal channel angular pressing. *Mater. Sci. Eng., A* **528**, 8179 (2011).
15. D. Terada, S. Inoue, and N. Tsuji: Microstructure and mechanical properties of commercial purity titanium severely deformed by ARB process. *J. Mater. Sci.* **42**, 1673 (2007).
16. Y.J. Chen, Y.J. Li, J.C. Walmsley, S. Dumoulin, and H.J. Roven: Deformation structures of pure titanium during shear deformation. *Metall. Trans. A* **41**, 787 (2010).
17. D.K. Yang, P. Cizek, P.D. Hodgson, and C.E. Wen: Microstructure evolution and nanograin formation during shear localization in cold-rolled titanium. *Acta Mater.* **58**, 4536 (2010).
18. N.R. Tao and K. Lu: Nanoscale structural refinement via deformation twinning in face-centered cubic metals. *Scr. Mater.* **60**, 1039 (2009).
19. A. Ghaderi and M.R. Barnett: Sensitivity of deformation twinning to grain size in titanium and magnesium. *Acta Mater.* **59**, 7824 (2011).
20. X.C. Zhao, W.J. Fu, X.R. Yang, and T.G. Langdon: Microstructure and properties of pure titanium processed by equal-channel angular pressing at room temperature. *Scr. Mater.* **59**, 542 (2008).
21. K.Y. Zhu, A. Vassel, F. Brisset, K. Lu, and J. Lu: Nanostructure formation mechanism of α-titanium using SMAT. *Acta Mater.* **52**, 4101 (2004).
22. W.L. Li, N.R. Tao, and K. Lu: Fabrication of a gradient nano-micro-structured surface layer on bulk copper by means of a surface mechanical grinding treatment. *Scr. Mater.* **59**, 546 (2008).
23. W. Chen, Q. Sun, L. Xiao, and J. Sun: Deformation-induced grain refinement and amorphization in Ti-10V-2Fe-3Al alloy. *Metall. Mater. Trans. A* **43**, 316 (2012).
24. K. Youssef, M. Sakaliyska, H. Bahmanpour, R. Scattergood, and C. Koch: Effect of stacking fault energy on mechanical behavior of bulk nanocrystalline Cu and Cu alloys. *Acta Mater.* **59**, 5758 (2011).
25. D.K. Yang, P. Cizek, D. Fabijanic, J.T. Wang, and P.D. Hodgson: Work hardening in ultrafine-grained titanium: Multilayering and grading. *Acta Mater.* **61**, 2840 (2013).
26. L. Xiao: Twinning behavior in the Ti–5at.% Al single crystals during cyclic loading along [0001]. *Mater. Sci. Eng., A* **394**, 168 (2005).
27. S-G. Hong, S.H. Park, and C.S. Lee: Role of {10-12} twinning characteristics in the deformation behavior of a polycrystalline magnesium alloy. *Acta Mater.* **58**, 5873 (2010).
28. T. Obara, H. Yoshinaga, and A. Morozumi: {1122} <1123> slip system in magnesium. *Acta Metall.* **21**, 845 (1973).
29. B. Li, S.P. Joshi, O. Almagri, Q. Ma, K.T. Ramesh, and T. Mukai: Rate-dependent hardening due to twinning in an ultrafine-grained magnesium alloy. *Acta Mater.* **60**, 1818 (2012).
30. C. Zener and J.H. Hollomon: Effect of strain rate upon plastic flow of steel. *J. Appl. Phys.* **15**, 22 (1944).
31. Y.S. Li, Y. Zhang, N.R. Tao, and K. Lu: Effect of the Zener–Hollomon parameter on the microstructures and mechanical properties of Cu subjected to plastic deformation. *Acta Mater.* **57**, 761 (2009).
32. J.W. Christian and S. Mahajan: Deformation twinning. *Prog. Mater. Sci.* **39**, 1 (1995).
33. I. Kim, J. Kim, D.H. Shin, X.Z. Liao, and Y.T. Zhu: Deformation twins in pure titanium processed by equal channel angular pressing. *Scr. Mater.* **48**, 813 (2003).
34. Q. Ma, H. El Kadiri, A.L. Oppedal, J.C. Baird, M.F. Horstemeyer, and M. Cherkaoui: Twinning and double twinning upon compres-

https://doi.org/10.1557/jmr.2014.19 Published online by Cambridge University Press

sion of prismatic textures in an AM30 magnesium alloy. *Scr. Mater.* **64**, 813 (2011).
35. Y.P. Li, S. Wu, H.K. Bian, N. Tang, B. Liu, Y. Koizumi, and A. Chiba: Grain refinement due to complex twin formation in rapid hot forging of magnesium alloy. *Scr. Mater.* **68**, 171 (2013).
36. I. Ulacia, N.V. Dudamell, F. Galvez, S. Yi, M.T. Perez-Prado, and I. Hurtado: Mechanical behavior and microstructural evolution of a Mg AZ31 sheet at dynamic strain rates. *Acta Mater.* **58**, 2988 (2010).
37. M.R. Barnett, Z. Keshavarz, A.G. Beer, and D. Atwell: Influence of grain size on the compressive deformation of wrought Mg–3Al–1Zn. *Acta Mater.* **52**, 5093 (2004).
38. D.H. Shin, I. Kim, J. Kim, Y.S. Kim, and S.L. Semiatin: Microstructure development during equal-channel angular pressing of titanium. *Acta Mater.* **51**, 983 (2003).
39. Y.J. Chen, Y.J. Li, J.C. Walmsley, S. Dumoulin, S.S. Gireesh, S. Armada, P.C. Skaret, and H.J. Roven: Quantitative analysis of grain refinement in titanium during equal channel angular pressing. *Scr. Mater.* **64**, 904 (2011).
40. T. Gorkaya, K.D. Molodov, D.A. Molodov, and G. Gottstein: Concurrent grain boundary motion and grain rotation under an applied stress. *Acta Mater.* **59**, 5674 (2011).
41. A.T. Lim, M. Haataja, W. Cai, and D.J. Srolovitz: Stress-driven migration of simple low-angle mixed grain boundaries. *Acta Mater.* **60**, 1395 (2012).
42. K.G.F. Janssens, D. Olmsted, E.A. Holm, S.M. Foiles, S.J. Plimpton, and P.M. Derlet: Computing the mobility of grain boundaries. *Nat. Mater.* **5**, 124 (2006).
43. D.L. Olmsted, E.A. Holm, and S.M. Foiles: Survey of computed grain boundary properties in face-centered cubic metals—II: Grain boundary mobility. *Acta Mater.* **57**, 3704 (2009).
44. Z. Guo, A.P. Miodownik, N. Saunders, and J.P. Schille: Influence of stacking-fault energy on high temperature creep of alpha titanium alloys. *Scr. Mater.* **54**, 2175 (2006).
45. Y.B. Chun, S.H. Yu, S.L. Semiatin, and S.K. Hwang: Effect of deformation twinning on microstructure and texture evolution during cold rolling of CP-titanium. *Mater. Sci. Eng., A* **398**, 209 (2005).
46. S.V. Zherebtsov, G.S. Dyakonov, A.A. Salem, V.I. Sokolenko, G.A. Salishchev, and S.L. Semiatin: Formation of nanostructures in commercial-purity titanium via cryorolling. *Acta Mater.* **61**, 1167 (2013).

https://doi.org/10.1557/jmr.2014.19 Published online by Cambridge University Press